Eocene-Oligocene intensification of the Deep Western Boundary Current in the North Atlantic Ocean

Andrew M. Parent[1,8], Kristin D. Chilton[2,3], Tim E. van Peer[4,5,6], Steven M. Bohaty[4,9], James F. Spray[4,10], Howie D. Scher[7], Paul A. Wilson[3], and Brian W. Romans[1]

1. Department of Geosciences, Virginia Tech, Blacksburg, VA, USA
2. Department of Civil and Environmental Engineering, Virginia Tech, Blacksburg, VA, USA
3. Department of Geology and Geography, West Virginia University, Morgantown, WV, USA
4. University of Southampton, Waterfront Campus, National Oceanography Centre Southampton, European Way, Southampton, SO14 3ZH, UK
5. Department of Earth Sciences, University College London, Gower Street, London, WC1E 6BT, UK
6. School of Geography, Geology, and the Environment, University of Leicester, University Road, Leicester, LE1 7RH, UK
7. Department of Earth, Ocean, and Environment, University of South Carolina
8. Now at: Shell U.S.A., Houston, TX
9. Now at: Institute of Earth Sciences, Heidelberg University, Heidelberg, Germany
10. Now at: School of Math and Science, The Community College of Baltimore County, 7201 Rossville Blvd, Baltimore, MD 21237, USA

Abstract

The role played by ocean circulation in major transitions in Earth's climate is debated. Here, we investigate the physical evolution of the Deep Western Boundary Current (DWBC) in the western North Atlantic Ocean through the late Eocene-to-mid Oligocene (35–26 Ma) using terrigenous grain size and geochemistry records of marine sediment cores. Our records cover the most pivotal transition in Cenozoic climate history, the Eocene-Oligocene Transition (EOT; ~33.7 Ma), when Earth first became sufficiently cool to sustain large ice sheets on Antarctica. To assess changes in deep-water circulation in the northwest Atlantic across the EOT, we assembled sortable silt (10–63 □m) grain-size and Nd, Hf, and Pb radiogenic isotope records at two Integrated Ocean Drilling Program (IODP) drill sites on the Newfoundland ridges (Sites U1406 and U1411). These records reveal an overall gradual increase in sortable silt abundance (SS%) at both sites with no change in sediment provenance. We interpret a steady, long-term invigoration of the DWBC, likely driven by deepening of the Greenland-Scotland Ridge and resultant enhanced inflow of waters sourced from deep-water production sites in the Nordic Seas to the North Atlantic Ocean. Our results do not support abrupt and widespread invigoration of bottom current activity in the North Atlantic synchronous with accelerated cooling and Antarctic ice growth at the EOT. Instead, our records suggest that the DWBC started to intensify before this pivotal event in Cenozoic climate

history (at ~35 Ma) and then further strengthened gradually across the EOT (~34 Ma) and through the early-to-mid Oligocene (~34–26 Ma).

1. Introduction

The role of oceanic thermohaline circulation in modulating Earth's climate has long been appreciated (e.g. Clark et al., 2002, and references therein) and has received considerable attention in recent years in light of ongoing anthropogenic climate change (e.g. Thornalley et al., 2018). Yet the relationship between ocean circulation and major changes in Cenozoic climate remains poorly understood. Atlantic Meridional Overturning Circulation (AMOC), the modern circulation system operating within the Atlantic Ocean basins, plays a major role in global climate and accounts for about one-third of global northward heat flux (Trenberth & Caron, 2001; Zickfield et al., 2007). AMOC constitutes a significant component of the global carbon cycle and climate system by effectively transporting heat from the atmosphere to the deep ocean (Kostov et al., 2014; Buckley & Marshall, 2016).

AMOC has been implicated in modulating the evolution of global climate for past climate transitions, for example leading into and following the Last Glacial Maximum (e.g. Du et al., 2020; Böhm et al., 2021). However, both the timing of AMOC initiation and the role played by AMOC in relation to the inception of a unipolar (Antarctic) glacial climate state (Zachos et al., 1992; Scher et al., 2011; Spray et al., 2019) at the Eocene-Oligocene Transition (EOT) are debated (Abelson & Erez, 2017; Elsworth et al., 2017; Hutchinson et al., 2021). Of particular interest is the evolution of North Atlantic Deep Water (NADW), the water mass formed in the northern North Atlantic and a major limb of the broader AMOC system. The timing and catalyst for production of the precursor to NADW, known as Northern Component Water (NCW), and its relation to the development of AMOC, especially prior to the Neogene, remains unclear (Sijp & England, 2004; Poore et al., 2006). For example, Sijp et al. (2011), in contrast to earlier hypotheses by Scher & Martin (2008), suggested that North Atlantic bathymetric changes were probably more critical to initiating southward transport of NCW than reorganization of circulation in the Southern Ocean. Additionally, recent studies based on radiogenic isotope (Coxall et al., 2018) and sea surface temperature (SST) records (Śliwińska et al., 2023) from the North Atlantic suggest significant oceanographic change occurred prior to the EOT.

The overflow of NCW into the North Atlantic Ocean and its incorporation into AMOC during the Neogene is suggested to have been heavily influenced by changes in the sill depth of the Greenland-Scotland Ridge (GSR) due to dynamic heat flux associated with the Icelandic Hot Spot (Wright & Miller, 1996; Poore et al., 2006; Parnell-Turner et al., 2015; Uenzelmann-Neben & Gruetzner, 2018). In this interpretation, deep-water exchange between the Nordic Seas and the North Atlantic Ocean was triggered by the cessation of spreading and subsidence of ridges, commonly referred to as tectonic gateways, separating the open North Atlantic from deep-water production sites to the north (e.g. Via & Thomas, 2006; Coxall et al., 2018). Deepening of the GSR is interpreted to have occurred in several phases during the mid-to-late Cenozoic, including during the early Oligocene (i.e. Davies et al., 2001; Via & Thomas, 2006; Abelson et al., 2008; Uenzelmann-Neben & Gruetzner, 2018; Straume et al., 2020). It is hypothesized that this deepening allowed outflow of NCW, ultimately leading to the hemispheric interchange of oceanic water masses and promoting early AMOC. Deepening of the GSR to a critical threshold depth triggers the initiation of outflow and incorporation of NCW to the Atlantic circulation system in the climate model simulations of Vahlenkamp et al. (2018a). However, other simulations emphasize the role of connectivity (or lack of) between the Arctic and Atlantic oceans as a key factor influencing early AMOC (e.g. Hutchinson et al., 2019; Straume et al., 2022).

Seismic-reflection data reveal a regional unconformity that spans the late Eocene through the mid Oligocene throughout parts of the deep North Atlantic basin (e.g. Mountain & Tucholke, 1985; Mountain & Miller, 1992; Wright & Miller, 1993). This unconformity, which in some areas of the western North Atlantic is erosional in nature (the 'Au' horizon of Mountain & Tucholke [1985]), has been interpreted to record invigoration of deep ocean currents during the latest Eocene to earliest Oligocene (Mountain & Tucholke, 1985). Early support for this interpretation came from suggestions that the inception of contourite drifts, sedimentary features deposited under the influence of deep ocean currents (Rebesco et al., 2014), in the North Atlantic also date to the EOT (e.g. Wold, 1994; Davies et al., 2001). However, Hohbein et al. (2012) suggested a much earlier onset of vigorous deep-water circulation near the early/middle Eocene boundary at ~48.5 Ma, based on seismic-reflection profiles in the Faeroe-Shetland Basin. This interpretation is supported by seismic-stratigraphic analysis and drillcore age calibration of sediment drifts of the Newfoundland ridges, which began accumulating at ~47 Ma (Boyle et al., 2017). Seismic-stratigraphic horizon A^u (Mountain & Tucholke, 1985; R4, Wright & Miller, 1993) is not well-

expressed or mapped in either of these drift systems, but the interpretations of Hohbein et al. (2012) and Boyle et al. (2017) are consistent with the main finding of Vahlenkamp et al. (2018) suggesting onset of NCW and modern-style AMOC in the Middle Eocene, predating the EOT by millions of years. Despite the valuable insights from these seismic-stratigraphic studies, there is little to no physical proxy data from drillcores that document the timing and development of NCW strength and variability during this time.

Here, we present terrigenous grain size and provenance records from two sites drilled during Integrated Ocean Drilling Program (IODP) Expedition 342 into the Newfoundland ridges drift complex, offshore Newfoundland, Canada. These records from IODP Sites U1406 and U1411 span the latest Eocene to the mid-Oligocene (35–26 Ma) and document grain-size characteristics and provenance of terrigenous clay and silt deposited under the influence of the DWBC on the J-Anomaly Ridge (JAR) [Site U1406] and the Southeast Newfoundland Ridge (SENR) [Site U1411]. Our data fill a major gap in knowledge for the EOT, because strata of latest Eocene–earliest Oligocene age are extremely rare in the North Atlantic (Mountain & Tucholke, 1985).

2. Geologic Setting

2.1 North Atlantic basin and modern oceanographic setting

Pangean rifting led to the opening of the North Atlantic, beginning in the middle Jurassic and Newfoundland was separated from Iberia by the Early Cretaceous (~128 Ma; Pe-Piper, 2007). Subsequent rifting progressed northward, ultimately opening the Labrador Sea and northeastern Atlantic Ocean (Pe-Piper, 2007). Today, the North Atlantic is a major locus of modern global oceanic circulation; North Atlantic Deep Water (NADW) is a key component of AMOC and moderates global water mass density properties (e.g. Fer et al., 2010). NADW is composed of water masses produced primarily in the Labrador Sea and Nordic Seas (e.g. Haine et al., 2008), including the Greenland-Scotland Overflow Water, Iceland Strait Overflow Water, and Labrador Sea Water. The confluence of these water masses creates the resultant properties of NADW (Haine et al., 2008), which then flows south along the western Atlantic basin as the DWBC (Fig. 1). The GSR is a prominent bathymetric high in the North Atlantic basin, separating the Nordic Seas to the north, and sites of modern deep convection and NADW production from the open North Atlantic Ocean to the south (Wright & Miller, 1996; Abelson et al., 2008).

130

131 *2.2 Newfoundland ridges drift complex*

132 The Newfoundland ridges drift complex is situated along the lower continental slope
133 offshore of the Grand Banks in ~3000–5000 m water depth. This contourite complex is large
134 (>70,000 km^2, up to >1 km thick) and comprised of several 'plastered' drifts (e.g. McCave &
135 Tucholke, 1986; Faguéres et al., 1999) that formed under the influence of bottom currents (Norris
136 et al., 2014a; Boyle et al., 2017). The active contourite phase of sedimentation on the
137 Newfoundland ridges broadly spans the interval between ~47 Ma (middle Eocene) and 3 Ma
138 (Pliocene) (Boyle et al., 2017). Contourites are effective archives of high-resolution
139 paleoceanographic records (e.g. Rebesco et al., 2014; McCave et al., 2017), not least because rates
140 of sedimentation are typically much higher than in pelagic settings (Stow et al., 2008). Thus, the
141 Newfoundland sediment drifts provide a long-term record of paleoceanographic change in the
142 North Atlantic Ocean spanning the mid to late Cenozoic.

143 We studied two IODP sites, U1406 (Norris et al., 2014b) and U1411 (Norris et al., 2014c).,
144 positioned at water depths of ~3800 m and ~3300 m, respectively (Figs. 1 and 2). The Eocene-
145 Oligocene paleodepth of Site U1406, located on the ENE-WSW trending JAR, is interpreted to be
146 ~450 m deeper than the WNW-ESE trending Site U1411, which is ~250 km northeast on the SENR
147 but well above the Paleogene calcite compensation depth (CCD). Both sites are carbonate-bearing
148 to carbonate-dominated, though Site U1406 sediments contain significantly higher carbonate
149 concentration than Site U1411 (Fig. 2). A lower Eocene through lower Miocene sedimentary
150 package was recovered at Site U1406, whereas the base of U1411 penetrates uppermost Eocene
151 sediments. Together, these two sites provide companion records leading into, across, and following
152 the EOT.

153

154 **3. Methods and Data**

155

156 *3.1 Site selection and suitability for sortable-silt reconstructions of current strength*

157 We use terrigenous grain-size records from Sites U1406 and U1411 to reconstruct the
158 evolution of the DWBC and interpret associated deep circulation history in the North Atlantic from
159 the latest Eocene to mid Oligocene (35–26 Ma), spanning the EOT interval (~34 Ma) (Fig. 2). We
160 focus on sortable silt, the terrigenous 10–63 μm fraction commonly used to assess changes in

bottom current intensity from the sedimentary record (McCave et al., 1995; McCave & Hall, 2006; Culp et al., 2021). The sortable silt proxy is based on the rationale that sediments are size-sorted according to bottom current strength. The lower limit of the sortable silt size range (10 μm) is necessitated by the tendency of fine silt and clay particles below this size to act cohesively. Sortable silt is especially applicable in deep-water settings, where contour currents are typically strong enough and persist over enough time to transport and deposit medium-to-coarse silt. The critical depositional velocity for sortable silt (i.e. the maximum velocity under which deposition will occur) in such deep-marine settings is ~18–20 cm/s (McCave et al., 2017), consistent with the long-term average velocity of bottom currents (e.g. Ledbetter, 1986).

First, we review the applicability of the sortable silt method to our study taking the limitations of the proxy into consideration (McCave & Hall, 2006). Migration of large-scale bedforms (10s of m amplitude; >km wavelength), which are common within drifts (e.g., Flood, 1988), over a single location can plausibly induce changes in the grain-size distribution unrelated to changes in current strength. Seismic-stratigraphic analysis of the Newfoundland ridges by Boyle et al. (2017) lends assurance that this is not an issue for our study, because there are no visible large-scale bedforms in the part of the drift studied (Fig. 2). Flow speeds may also vary within the current itself, due to local interactions with bathymetric obstacles (e.g., seamounts) and eddies (e.g. McCave et al., 2006). Therefore, lateral and vertical shifts in flow axis can result in changes in energy conditions, and the associated grain-size distribution, at a given location that are unrelated to temporal changes in overall current strength. Our study was designed to addresses this issue by developing records from two sites in different water depths, separated by ~250 km distance, and positioned on different bathymetric highs (Figs. 1 and 2), allowing for comparison between sites and more confidence in identifying long-term trends. Also problematic is the potential for input of sediment transported by other processes, such as ice rafting or sediment gravity flows. At Sites U1406 and U1411, there is no evidence for the presence of turbidity current deposits (i.e. graded beds are absent) in keeping with the bathymetric isolation of the Newfoundland ridges from downslope sediment transport from the adjacent Grand Banks (Fig. 1) and this is a primary reason that IODP Exp 342 targeted these drifts (Norris et al., 2014a). Work by Spray et al. (2019) at Sites U1406 and U1411 reports trace amounts of very fine-grained (63–125 μm) terrigenous well-sorted sand, which is interpreted to have been transported by bottom

currents (not ice-rafting as hypothesized shipboard during IODP Exp 342, Norris et al., 2014a), supporting the interpretation that drift architecture reflects long-term dynamics of the DWBC.

3.2 Site lithology, age models, and sediment accumulation rates

Sites U1406 and U1411 contain relatively continuous and, in the case of Site U1411, significantly expanded, EOT sections (Fig. 2; Norris et al., 2014a). The Eocene-Oligocene sections at Sites U1406 and U1411 contain calcareous nannofossil ooze and clay, with variable amounts of terrigenous clay and silt (Fig. 2; Norris et al., 2014b; Norris et al., 2014c). Silty clay and very fine sand are common at Site U1411. The analyzed Site U1406 sediments contain larger proportions of $CaCO_3$ wt.% (mean = 54 wt.%) compared to Site U1411 (mean = 28 wt.%) (Fig. 2). Age models were constructed using biostratigraphic and magnetostratigraphic age constraints from Norris et al. (2014c) for Site U1411 and from Norris et al. (2014b) and van Peer et al. (2017) for Site U1406 (Fig. 3). A recent review of the EOT by Hutchinson et al. (2021) defines key boundaries across the ~750 kyr duration of the event that are used in this paper: extinction of *D. saipanensis* at 34.44 Ma marking the onset of the EOT, the Eocene-Oligocene Boundary (EOB) at 33.9 Ma, the base of Chron C13n at 33.705 Ma, and the earliest Oligocene oxygen isotope step (EOIS), coincident with the increase in $\delta^{18}O$ that marks the event at 33.65 Ma (see Table S1 for depth positions of these important biostratigraphic and magnetostratigraphic datums). We note however that there are some uncertainties in our age models. For example, within the EOT interval of Site U1406 the last occurrence of the calcareous nannofossil *D. saipanensis* (Norris et al. 2014b) and the base of Chron C13n are identified at nearly the same stratigraphic level, which could indicate the presence of a hiatus in the early part of the EOT (Fig. 3). We use the refined Site U1406 age model of van Peer et al. (2017), which does not include a significant hiatus in the EOT interval, but acknowledge that our interpretations during the latest Eocene of Site U1406 are dependent on the inferred the continuity of the record within this interval. Further refinement of the shipboard calcareous nannofossil biostratigraphy is required to clarify this issue.

Mass-accumulation rates (MAR) were calculated using site-specific linear sedimentation rates (LSR) and dry bulk densities (ρ_b) based on interpolation from shipboard physical properties measurements (Norris et al., 2014a).

$$MAR\ (g/cm^2/kyr) = LSR\ (cm/kyr) * \rho_b\ (g/cm^3) \quad \text{Eq. 1}$$

Terrigenous MARs were determined by multiplying MAR by the fraction of non-carbonate material (i.e., residue after carbonate dissolution) at a given interval for that sample (Fig. 4). 329 samples (137 from Site U1406; 192 from Site U1411; Fig. 2) of ~10 cm^3 were selected from sediment cores for grain-size analysis. Samples from both sites span the interval between 35–26 Ma, with a higher sampling density within the EOT interval at both sites (Fig. 2). Temporal resolution ranges from 10 kyr within the EOT to 100 kyr in other intervals. A mid-Oligocene intra-formational slump interval at U1406 identified by van Peer et al. (2017) (~182-176 m CCSF) results in a ~1.8-Myr gap in our record, from ~29.0 to ~27.2 Ma (Fig. 3). We did not analyze any samples from this interval, and the extent of the slumped interval is indicated by shaded interval in our data plots.

3.3 Sample preparation and grain-size measurement

A Micromeritics SediGraph 5120 was used to generate mass abundance data of the <63 µm range and grain-size metrics of the 1–63 µm range of the terrigenous fraction of the bulk sediment. The SediGraph measures sediment concentration and particle settling velocity within an X-ray monitored suspension chamber and, by Stoke's Law, determines particle size (Coakley & Syvitski, 1991). Several studies have indicated that the SediGraph is a preferable method for the analysis of clay-rich sediments because it uses the physical process of sedimentation rather than other, indirect techniques (see McCave et al., 2006 for a review). To isolate the terrigenous fraction, $CaCO_3$ (e.g., dominated by coccoliths with some foraminifera; Norris et al., 2014b; Norris et al., 2014c) was removed following the procedures of Nicolo & Dickens (2006), via two-hour sessions of digestion in a 25% acetic acid solution, performed twice, during which samples were constantly agitated on a rocking table. Samples did not require chemical treatment for removal of biogenic opal because radiolaria and diatoms are absent or in negligible amounts in these sediments in our study interval (Norris et al., 2014b; Norris et al., 2014c).

Following $CaCO_3$ removal and freeze drying, samples were weighed to determine the mass percentage of the carbonate fraction that was removed prior to SediGraph analysis. They were then re-hydrated using NanoPure (18.2 MΩ-cm) water, after which samples were sieved at 63 µm to obtain the fine fraction for grain-size analysis. A solution of 0.5% tetrasodium pyrophosphate (TSPP) was used during sieving to prevent flocculation of samples. The coarse fraction was left to

dry on the sieve in an oven at 50°C, then weighed to determine mass percentage of >63 μm fraction (% sand). The fine (<63 μm) fraction was left to settle in beakers for five days, at which point excess liquid was siphoned off and samples were freeze dried. A 1.0 g aliquot of each fine fraction was removed for analysis in the SediGraph. Immediately prior to analysis, each sample was dispersed in 65 mL of 0.5% TSPP and sonicated for 15 minutes at 40 kHz to aid in disaggregation of clays. Our analysis is focused on the <63 μm fraction; see Spray et al. (2019) for analysis and interpretation of the >63 μm fraction from Sites U1406 and U1411.

3.4 SediGraph data processing and calculation of grain-size metrics

SediGraph output data (cumulative frequency tables) were imported into customized Python scripts for processing and calculation of the desired statistical metrics. Raw data were mathematically corrected to account for occasional cumulative distribution function (CDF) values >1.0 that resulted from SediGraph measurement. Sortable silt percent (SS%) was calculated as the proportion of mass in 10–63 μm range. Mean sortable silt ($\overline{SS}$) was calculated following McCave & Andrews (2019) from the natural log transformed bin sizes, $\theta_i = \ln(d_i)$ where d_i is the percent finer than the bin edge in microns, in the context of the total grain size distribution of a sample's output by the SediGraph. $\overline{SS}$ is thus defined as:

$$\overline{SS} = e^{\theta_i} \quad \text{Eq. 2}$$

with θ_m defined as:

$$\theta_m = \sum_{i=1}^{n} \overline{\theta}_i f_{ss,i} \quad \text{Eq. 3}$$

where θ_i is equivalent to the "natural log of the bin's geometric mid-point diameters" as discussed by McCave & Andrews (2019), and $f_{ss,i}$ is the fraction of material associated with the SS size range (10–63 μm) in bin i (i=1 is associated with the bin whose lower edge is 10 μm and i=n is associated with the bin whose upper edge is 63 μm). We report SS% in addition to $\overline{SS}$ and emphasize trends in SS% as a bottom-current indicator to mitigate the uncertainty associated with $\overline{SS}$ calculation in deposits with very low (<5%) SS abundance (Bianchi et al., 1999).

Moving averages for $\overline{SS}$ and SS% were calculated by computing the average of the four surrounding values for each data point. To better compare the long-term trends of Sites U1406 and U1411 mass abundance data, plots are scaled to their respective minima and maxima (Fig. 4). Plots showing the distribution of $\overline{SS}$ and SS% data (as combined density curve and boxplot) for the Eocene and Oligocene were constructed to compare sites (Fig. 5).

3.5 Detrital provenance data

For sequential extraction of the detrital terrigenous fraction, 1–5 mg sediment samples from Site U1411 were freeze dried and weighed. Samples were rehydrated in 18 MΩ-cm water and mechanically disaggregated on a shaker table overnight. To remove the carbonate fraction, liquid was extracted after centrifugation and 1M acetic acid was added to the samples at 35 ml/g of sediment. After resuspending the sediment using a vortex mixer, samples were rocked on a rocking tray for 12 hours. Vials were degassed regularly. After centrifugation the supernatant was discarded and the samples were rinsed 3 times with 18 MΩ-cm water with centrifugation and resuspension in between. Samples were then leached with $MgCl_2$ to remove adsorbed ions from the carbonate removal step. Supernatant was discarded and samples were rinsed three times with 18 MΩ-cm water with centrifugation and resuspension in between. The dispersed FeMn oxyhydroxide fraction, or coating, was removed using a two-phase oxidative leach with hydroxylamine hydrochloride and EDTA. The first (weak) leach was retained for future study. Following the second (strong) leach the supernatant was discarded and the samples were rinsed 3 times with 18 MΩ-cm water with centrifugation and resuspension in between. Samples were then treated with $MgCl_2$ to remove adsorbed ions from the dispersed FeMn removal step. Supernatant was discarded and samples were rinsed three times with 18 MΩ-cm water with centrifugation and resuspension in between. After a final rinse in methanol, the sample was dried and weighed.

500 mg of the residual detritus was transferred to steel jacketed Teflon bombs and digested in HF/HNO_3. In a metal-free clean room the sample digests were heated to dryness in Teflon vials, reconstituted in HCl, and processed through cation exchange columns to separate Hf and Nd for mass spectrometry. Hf and Nd isotopes were measured on a ThermoFisher Neptune multi-collector inductively coupled plasma mass spectrometer (MC-ICPMS) with the Plus upgrade. Measurements were made in static mode and samples were introduced to the plasma via an Apex-Q with a 50 ul/min Teflon nebulizer. Isotope ratios were corrected for instrumental mass bias using

$^{179}Hf/^{177}Hf$ = 0.7325 and $^{146}Nd/^{144}Nd$ = 0.7219. The $^{177}Hf/^{176}Hf$ ratios were normalized to JMC Patchett = 0.282160 and $^{143}Nd/^{144}Nd$ ratios to JNdi-1 = 0.512115.

We also explored changes in the provenance of the detrital fraction within the studied interval using $^{206}Pb/^{204}Pb$, $^{207}Pb/^{204}Pb$, and $^{208}Pb/^{204}Pb$ isotope ratios of detrital feldspars originally reported in Spray et al. (2019). Specifically, 350–500 sand-sized (>63 μm) feldspar grains were hand-picked from 24 samples from Site U1411. The grains from each sample were then digested *en masse*, following the methods of Taylor et al. (2015), and column chemistry (AG1x8 anion exchange resin) was performed to isolate Pb, following Baker et al. (2004). Pb isotopes were then analyzed using a ThermoFisher Neptune MC-ICPMS). The obtained values were corrected for instrumental mass fractionation using the SBL74 double spike method (Taylor et al., 2015). Repeated measurements of the Pb isotope reference NBS981 (>100 measurements during four years prior to analysis) gave a $^{206}Pb/^{204}Pb$ value of 16.9400 ± 0.0023, $^{207}Pb/^{204}Pb$ of 15.496 ± 0.0026, and $^{208}Pb/^{204}Pb$ of 36.7124 ± 0.0076. The given values for NBS981 are $^{206}Pb/^{204}Pb$ of 16.9418 ± 6, $^{207}Pb/^{204}Pb$ of 15.500 ± 6, and $^{208}Pb/^{204}Pb$ of 36.7265 ±19 (Baker et al., 2004).

4. Results

4.1 Site U1406

At Site U1406, terrigenous silt % increases abruptly at ~34.7 Ma immediately prior to the EOT and then decreases steadily to ~33.9 Ma (Fig. 4a). A subsequent marked increase at the EOIS (33.65 Ma; Hutchinson et al., 2021) is followed by a minor decrease. The silt % remains elevated until ~30 Ma, after which it sharply decreases and then fluctuates into the mid Oligocene (~29.3 to 26 Ma). SS% steadily increases from the latest Eocene into the EOT interval and, similar to silt %, decreases in the middle of the EOT interval before increasing abruptly at the EOIS (Fig. 4b). This shift at the EOIS is followed by a modest, yet notable, increase through the early-to-mid Oligocene interval (~33 to 29 Ma). $\overline{SS}$ exhibits two abrupt increases during the EOT (Fig. 4c), but the pre- and post-EOT record exhibits little change and does not track the increasing trends of silt % and SS%. Overall, SS% is higher in the Oligocene than the Eocene at Site U1406 and is much less variable in the Oligocene (Fig. 5), though sample resolution is generally lower in the Oligocene. $\overline{SS}$ in the Eocene is slightly higher on average than in the Oligocene (Fig. 5).

345 *4.2 Site U1411*

346 At Site U1411, silt % increases abruptly and significantly at ~34.5 Ma immediately
347 preceding the base of the EOT. This increase continues, overall, through most of the EOT before
348 decreasing across the EOIS (Fig. 4a). The post-EOT record at Site U1411 is characterized by a
349 gradual increase in silt % through the early to mid Oligocene (~33.5 to 26 Ma). SS% similarly
350 increases sharply near the base of the EOT (Fig. 4b). A steady decrease to ~34.0 Ma is followed
351 by an increase to ~33.8 Ma, after which SS% again decreases across the EOIS to ~33.1 Ma. Similar
352 to the silt % record, SS% exhibits a protracted increase through the early to mid Oligocene. The
353 $\overline{SS}$ record at Site U1411 is variable, especially in the pre-EOT section, but shows a systematic
354 increase over the entire studied interval (Fig. 4c). Both SS% and $\overline{SS}$ are higher in the Oligocene
355 than the Eocene at Site U1411 (Fig. 5).
356
357 *4.3 Detrital provenance data*

358 Our provenance data from Site U1411 does not extend across the entire 35–26 Ma study
359 interval and, thus, is displayed in Figure 6, which focuses on the EOT and time intervals
360 immediately preceding and after (35–32.5 Ma). Broadly, εHf, εNd, and Pb/Pb data do not exhibit
361 any well-defined trends. However, a transient, less-radiogenic spike at the end of the EOT is
362 exhibited by εNd, coupled with a peak in $^{206}Pb/^{204}Pb$. The detrital lithogenous εNd and εHf data
363 do not exhibit a long-term trend, nor any protracted inflections associated with the first $\delta^{18}O$ step
364 (33.9 Ma; Hutchinson et al., 2021) or the EOIS. A one-point outlier in εNd values coincides with
365 the EOIS.
366
367 *4.4 Intersite comparison of sortable silt mass abundance and terrigenous mass-accumulation rates*

368 Coupling terrigenous grain-size records from two IODP study sites at different paleodepths
369 affords a regional, robust perspective of long-term change in bottom-current conditions. Here, we
370 summarize and compare the SS% records exhibited at both Sites U1406 and U1411 from the late
371 Eocene to the late Oligocene (Fig. 4b). The 4-point moving averages superimposed on the data
372 reflect the longer-term trends. SS% decreases between ~34.2 and 34.0 Ma at Site U1406 before
373 increasing slightly to the EOIS. At Site U1411, SS% increases sharply from ~34.2 Ma to the EOB,
374 before decreasing steadily to the EOIS. SS% trends notably diverge during the EOT and appear to
375 exhibit an anti-phase relationship from ~34.2 Ma to the EOIS (Figs. 4a and 6a). Post-EOT, both

records gradually increase through the early Oligocene into the mid Oligocene. These changes in SS% suggest a variable bottom-current flow speed history preceding and throughout the EOT, followed by an increase at both sites from the EOIS through the top of our study interval in the mid Oligocene.

Terrigenous MARs at both sites exhibit little change within the pre-EOT interval, with the exception of an anomalously high value at Site U1411 at 34.5 Ma (Fig. 4d). Site U1411 exhibits an abrupt increase in terrigenous MAR at 34.0 Ma, whereas terrigenous MAR at Site U1406 decreases at this same time. Terrigenous MAR at Site U1406 steadily decreases starting at ~34.2 Ma before increasing abruptly at the EOIS, whereas Site U1411 exhibits an increase at ~34.1 Ma before mimicking the steady decrease at Site U1406. Terrigenous MAR at Site U1411 decreases appreciably at the EOIS and then both sites exhibit a steady increase, similar to the SS% records, in the post-EOT period between ~33.6–32.5 Ma.

5. Discussion

5.1 Controls on terrigenous grain-size records in Newfoundland ridges contourite drifts

Before we can assess the imprint of the DWBC on our records we must first consider the influence of other processes that may have influenced our terrigenous grain-size data. First, we might expect an increase in sediment supply to have been associated with glacioeustatic sea-level fall in response to the growth of ice sheets on Antarctica (e.g., Miller et al., 2020). For example, during sea-level fall, an addition of coarser material derived from coastal and shelf staging areas may have been transported via sediment gravity flows further into the deep basin (e.g., Posamentier et al., 1991), intercepted by the DWBC and incorporated into the construction of contourites on the Newfoundland ridges. SS% increases gradually and systematically at both sites over a multi-million-year timescale and $\overline{SS}$ is generally higher in the Oligocene compared to the Eocene (Figs. 4, 5, 6, and 7). Spray et al. (2019) show that sand (>63 μm) abundance increases in the earliest Oligocene at both Sites U1406 and U1411, which may support a sea-level-lowstand driver of sediment supply interpretation. However, the onset of the long-term coarsening trend in Site U1411 pre-dates the beginning of the EOT (Fig. 6). Moreover, the systematic coarsening in both of our records continues for millions of years post-EOT (Fig. 7). Thus, a longer-term process is the more likely driver of the coarsening trend that we document than sea-level fall-induced change,

and we note that Spray et al. (2019) interpreted bottom current intensity/activity to have been the fundamental process controlling sand abundance in their records.

A second process with the potential to alias our records is changing sediment source through time. To address source-area changes, we studied the radiogenic isotope composition (εNd, εHf) of the bulk detrital fraction and $^{206}Pb/^{204}Pb$ in hand-picked feldspar grains at Site U1411 (Figs. 6f and 6g). Detrital provenance data from Site U1411 reveal no significant changes in sediment source area across the EOT. Although εNd exhibits a transient excursion to less-radiogenic values associated with the EOIS, neither εHf nor $^{206}Pb/^{204}Pb$ data reveal an abrupt and sustained shift coincident with the EOT (Fig. 6). Overall, εHf and εNd display little variability across the EOT and $^{206}Pb/^{204}Pb$ data show no discernible overall trend. Here, we emphasize the lack of systematic change in these provenance metrics and do not analyze them for the purpose of interpreting specific source areas (see Spray et al. [2019] for analysis and interpretation of sediment source areas for these drift deposits).

5.2 Long-term invigoration of DWBC in response to GSR deepening and overflow

The onset of contourite sedimentation is well constrained prior to 36 Ma on the Newfoundland ridges (Boyle et al., 2017) and elsewhere in the North Atlantic (Hohbein et al., 2012), but the relative intensity of the DWBC cannot be constrained by seismic stratigraphy alone. Our terrigenous grain-size records reveal a gradual and long-term (35–26 Ma) increase in SS% at two sites in different water depths in the Newfoundland ridges drift complex (Figs. 4 and 7). This pattern of change suggests a protracted strengthening of the DWBC pre-, syn-, and post-EOT. Although we emphasize the abundance of sortable silt (SS%) in Figures 6 and 7, it is worth noting that $\overline{SS}$ is also generally coarser in the Oligocene compared to the Eocene (Fig. 5). Our sedimentological records highlight the difference in timescales of DWBC strengthening (multiple million years) versus the relatively abrupt climate shift associated with the EOT (hundreds of thousands of years). These physical proxies reveal a steady increase the strength of deep circulation from the EOT through the mid Oligocene, potentially representing the gradual establishment of AMOC. Additionally, our records suggest that widespread invigoration of deep-water circulation previously interpreted to coincide with the EOT based on regional seismic-stratigraphic mapping across the western North Atlantic (e.g., Mountain & Tucholke, 1985; Wright & Miller, 1993) could have occurred later in the Oligocene.

438 The long-term and gradual trends in our data appears inconsistent with a major influence
439 exerted by faster-acting processes associated with onset of significant Antarctic glaciation.
440 Tectonic forcing has been proposed as an underlying control on late Eocene to EOT ocean
441 circulation changes in the South Atlantic (Borelli et al., 2014; Langton et al., 2016) and Southern
442 Ocean (Scher & Martin, 2006; Scher et al., 2015; Scher, 2017). In the North Atlantic, the
443 tectonically driven deepening and shoaling of the Greenland-Scotland Ridge (GSR) during the
444 Cenozoic has been invoked as a major control on deep-water production and flow from the
445 shallower Nordic Seas southward into the deeper North Atlantic (Davies et al., 2001; Via &
446 Thomas, 2006; Abelson et al., 2008; Hutchinson et al., 2019). During the Neogene, for example,
447 Wright & Miller (1996) and Poore et al. (2006) showed that temporal variability in Northern
448 Component Water (NCW) production correlates with well-documented vertical motions of the
449 GSR during the middle Miocene through Pliocene (i.e., when the GSR subsided, overflow of NCW
450 into the North Atlantic was enhanced). The Uenzelmann-Neben & Gruetzner (2018) review of
451 GSR overflow chronology, which does not include information from the Newfoundland ridges
452 drifts, indicates that the GSR subsided from ~32 to 23 Ma, suggesting that deep waters sourced
453 from the Nordic Seas may have contributed to the observed bottom-current invigoration in the
454 Oligocene part of our record.
455 Another potential source of deep/bottom water that could have influenced sediment
456 transport on the Newfoundland ridges, but is not directly associated with a tectonic control, is from
457 the Labrador Sea. Previous studies investigating potential sources of NCW in the latest Eocene
458 suggested that convective overturning in the Labrador Sea may have led to enhanced bottom-water
459 activity during this time (Borelli et al., 2014). Deep Sea Drilling Program (DSDP) Site 112 in the
460 southern Labrador Sea shows a change from dominantly clay to a higher proportion of silt in the
461 Early Oligocene that is associated with a prominent seismic reflector interpreted to represent
462 invigoration of bottom-water flow (Miller et al., 1982). More recent work on Ocean Drilling
463 Program (ODP) Site 647 reveals a significant decrease in deep-water agglutinated foraminifera at
464 the Eocene-Oligocene boundary (Kaminski & Ortiz, 2014) and a modest increase in sedimentation
465 rate coincident with the EOT (Firth et al., 2013), which may represent more vigorous ocean
466 circulation. However, Coxall et al. (2018) and Vahlenkamp et al. (2018a), based on isotope records
467 and oceanographic modeling, respectively, suggest that the deep water in the latest Eocene North

Atlantic was sourced from the Nordic Seas, which implies the GSR sill was sufficiently deep to promote north-to-south flow by this time.

Neogene records from the North Atlantic show that Labrador Sea-sourced deep water was more prevalent when a shallower GSR sill prevented overflow from the Nordic Seas and was significantly diminished when GSR overflow was active (Poore et al., 2006), suggesting that a similar dynamic may have been established in the late Paleogene. We interpret that the long-term invigoration of the DWBC evident in our physical record was driven by progressive deepening of the GSR, which permitted enhanced overflow of NCW into the North Atlantic and associated intensification of the DWBC. This multiple-million-year timescale increase in bottom-current energy might reflect the onset of different segments of the GSR, which have different sill depths and, thus, could have had different timings of overflow. For example, the southeasternmost segment of the GSR, the Faroe-Shetland Channel, is the deepest part of the ridge (Vogt, 1972) and has been hypothesized to have been an important oceanic gateway connecting the Nordic Seas with the North Atlantic from the earliest Oligocene (Davies et al., 2001) or as old as the Early-Middle Eocene (Hohbein et al., 2012). However, the position of the Newfoundland ridges drifts, which are down-current from the confluence of multiple deep-water sources, precludes the ability to test that hypothesis directly.

5.3 Changes in the intensity and depth of the DWBC associated with the EOT

Our records from Sites U1406 and U1411 also provide an opportunity to address a long-standing question in Cenozoic paleoceanography: Did North Atlantic deep circulation intensify abruptly at the EOT? At Site U1411, our record shows that the observed long-term increase in SS% begins well before the Eocene-Oligocene Boundary and prior to the beginning of the EOT (Fig. 6). At Site U1406, there is little change in SS% during the pre-EOT and through most of the EOT with a notable, but transient, increase just after the EOIS (Fig. 6). At Site U1411, our record shows a modest decrease in SS% from the EOB through the end of the EOT with coarsening resuming at Site U1411 in the post-EOT time period (from ~33.3 Ma and younger) (Fig. 6). Thus, our terrigenous grain-size data do not support an interpretation of regionally synchronous intensification of the DWBC associated with global cooling and rapid growth of the Antarctic Ice Sheet across the EOT. The lack of a regional seismic-stratigraphic horizon in the Newfoundland

ridges drifts at this level (Boyle et al., 2017) supports our proxy-based interpretation of no major change in the drift system at or near the time of the EOT.

Although our proxy records spanning the EOT do not exhibit a synchronous response, we note that these two sites are at different modern water depths within the same overall contourite drift system and can therefore be used to investigate changes in bottom-current behavior as a function of paleo-water depth (e.g., see Norris et al., [2014a] regarding the similar subsidence histories of these two sites). We hypothesize that the earlier onset of coarsening at the shallower Site U1411 (~34.5 Ma) relative to the deeper Site U1406 (~33.7 Ma) represents bottom-current invigoration followed by deepening (or potentially spanning a larger depth range). In this interpretation, the strength of the bottom current in shallower parts of the drift system (~3,300 m modern water depth) increased ~800 kyr before the deeper parts (~3,800 m modern water depth). Additionally, the relationship between SS% and terrigenous MAR (Fig. 6b) observed at Sites U1406 and U1411 may also suggest depth-dependent changes in bottom currents during this period. For example, the EOIS at Site U1406 shows an increase in both SS% and terrigenous MAR, which likely represents a stronger bottom current transporting both coarser and more terrigenous sediment to the site. In contrast, an increase in terrigenous MAR at Site U1411 coincides with an increase in SS% at ~34.0 Ma, but then followed by a significant decrease in terrigenous MAR at the EOIS, which is accompanied by little change in SS%. Overall, the variability at the shallower Site U1411 of both SS% and terrigenous MAR after the initial coarsening suggests a more complex evolution of the physical current during the EOT at this location and depth.

In summary, we do not see evidence for an abrupt and basin-wide invigoration of bottom currents in the North Atlantic associated with the EOIS. In fact, our data suggest an increase in DWBC intensity that starts prior to the beginning of the EOT in the shallower site and evolves through the EOIS. Similarly, Coxall et al. (2018) interpret that NCW export began about 500 kyr before the beginning of the EOT in North Atlantic sites. Recent modeling-focused studies have emphasized the importance of Arctic-Atlantic connections and the role of associated freshwater influx (or lack of) into the open Atlantic prior to and during the EOT as well. For example, Hutchinson et al. (2019) concluded that closure of the Arctic-Atlantic connection could have led to increased salinity in the North Atlantic and initiation of AMOC whereas Straume et al. (2022) highlight the interplay of changes in both Arctic-Atlantic connectivity and GSR sill depth. Regarding sea surface temperature (SST) records, Śliwińska et al. (2023) show that the southern

Labrador Sea (ODP Site 647) started to cool ~500 kyr prior to the beginning of the EOT whereas the lower-resolution SST data from Liu et al. (2018) from nearby Site U1404 shows little change during the EOT, after which it cools during the Oligocene (Fig. 7). The earliest Oligocene appearance of palynomorphs linked to surface-water cooling at multiple sites on the Newfoundland ridges (Egger et al., 2016) is generally consistent with these findings. Śliwińska et al. (2023) and other recent studies have discussed the apparent contradiction of cooling SSTs coinciding with increasing AMOC. We note that although our grain-size record shows an increase during this important transition, the SS% in terms of an absolute abundance is quite low, which suggests relatively weak circulation intensity during this time. SST records at Site U1406 indicate a cool early to mid Oligocene relative to late Oligocene and Miocene (Guitián et al., 2019) but we note that their record begins at 30 Ma and does not capture the EOT changes. Additional work at higher resolution, including more sites, and comparison with site-specific benthic oxygen isotope data (e.g. density variability of water masses; Lynch-Stieglitz et al. [1999]) is needed in order to quantify the variability and trends revealed by our data set.

These recent studies, combined with our data set emphasizing the physical behavior of bottom currents, points towards considerable spatiotemporal variability of North Atlantic circulation leading up to and during the EOT, which, as is discussed above, became more established and potentially more volumetrically significant (i.e., covering a larger depth range) as the Oligocene progressed. The extent to which latest Eocene DWBC strengthening may have been a forcing for EOT oceanographic change is difficult to evaluate because our record does not extend significantly into pre-EOT intervals. Nonetheless, if changes in ocean circulation that initiated in the Eocene contributed to climatic change at the EOT it would have necessarily been a threshold response.

6. Conclusion

We present terrigenous grain-size and detrital provenance data from IODP Exp 342 Sites U1406 and U1411 on the Newfoundland ridges drift complex. These contourites provide a high-resolution sedimentary archive from the latest Eocene through mid-Oligocene interval. Terrigenous sortable silt (10–63 μm) data in our new record shows a gradual coarsening between 35 and 26 Ma at both sites. At shorter timescales, and in the context of the Eocene-Oligocene Transition (EOT), the most pivotal climate transition of the Cenozoic, our records suggest that

change in bottom currents were not synchronous at both sites. The inception of the coarsening signal predates the beginning of the EOT in Site U1411 and continues to the top of our record in the mid-Oligocene at both sites. We rule out sediment source changes as an explanation for the grain-size trends due to unvarying provenance indicators across the EOT. We interpret the coarsening of sortable silt in our records to indicate steady and long-term invigoration of the Deep Western Boundary Current (DWBC) over a multi-million-year timescale. This timescale of deep circulation change is consistent with tectonic drivers and evolution of the North Atlantic in the late Paleogene. Specifically, the deepening of the Greenland-Scotland Ridge (GSR) likely permitted increased overflow of Northern Component Water (NCW) produced in the Nordic Seas into the North Atlantic, representing a protracted assembly of AMOC.

Acknowledgments

BWR acknowledges an IODP Exp 342 post-expedition award for allowing an initial data set to be generated several years ago. AMP and KDC acknowledge the Virginia Tech Dept. of Geosciences for teaching assistantship support while they did this work. There is neither any real nor any perceived financial conflicts of interests for any authors. We thank the scientists and crew of IODP Expedition 342.

Data Availability Statement

This research used samples and data provided by the Integrated Ocean Drilling Program (IODP). Shipboard data from IODP Exp 342 are available at Norris et al. (2014a,b,c). The grain-size data generated for this study are openly available on Pangaea at Parent et al. (20XX).

Figure Captions

Fig. 1: (A) Bathymetric map of Newfoundland ridges drift complex, offshore Canada, showing location of new terrigenous grain-size data reported in this study from Sites U1411 and U1406 (from IODP Exp 342). Approximate path and depth range of modern Deep Western Boundary Current (DWBC) annotated by red arrows. (B) Inset showing expanded view of the northern North Atlantic Ocean, southern Labrador Sea, the Greenland-Scotland Ridge (GSR), and Greenland-Norwegian Sea. Part A designated by dashed white box. Note location of other sites with published data referenced in the text. Maps generated using http://www.geomapapp.org/

Fig. 2: Seismic-stratigraphic and lithologic context for IODP Sites U1406 and U1411 and associated analyzed samples. (A) Seismic-reflection profile (Line 5), including horizon interpretation from Boyle et al. (2017), showing Site U1406 location. (B) Seismic-reflection profile (Line 25), including horizon interpretation from Boyle et al. (2017), showing Site U1411. Key to seismic-stratigraphic horizon colors for both profiles. (C) Summary of Site U1406 and (D) of Site U1411, both showing core recovery, lithology, general age, and shipboard $CaCO_3$% information (from Norris et al., 2014b; Norris et al., 2014c). Stratigraphic distribution of samples with the EOT (Eocene-Oligocene Transition) interval, per Hutchinson et al. (2021), shown in red.

Fig. 3: Age models for IODP Sites U1406 and U1411 constructed using biostratigraphic and magnetostratigraphic tie points (Norris et al., 2014b; Norris et al., 2014c; van Peer et al., 2017). From left to right: magnetostratigraphy of Site U1406, depth-age tie points used in this study, and magnetostratigraphy of Site U1411. Question mark (?) denotes interval where paleomagnetic age constraint is less clear. Magnetostratigraphies are correlated to the Geomagnetic Polarity Time Scale (Gradstein et al., 2012) across the bottom of the plot.

Fig. 4: Terrigenous grain-size data. (A) Mass abundance of silt (4-63 □m fraction). (B) Mass abundance of sortable silt (10-63 □m fraction). (C) Mean sortable silt (mean diameter of 10-63 □m fraction). Parts A-C have a 4-point moving average superimposed on data. (D) Terrigenous (non-carbonate) mass accumulation rates. U1406 (red) and U1411 (black) for all panels. Eocene-Oligocene Transition (EOT) and earliest Oligocene oxygen isotope step (EOIS) as defined by Hutchinson et al. (2021) shown.

Fig. 5: Violin plots (mirror-image density curves) with boxplot overlay of terrigenous (A) sortable silt (10-63 μm) mass % and (B) mean sortable silt for Sites U1406 and U1411 subdivided into Eocene versus Oligocene (using Eocene-Oligocene boundary of 33.9 Ma). Boxplots show interquartile range (white fill) and median (vertical line). Annotation denotes standard deviation and number of data points.

Fig. 6: Multi-proxy record across the Eocene-Oligocene Transition (EOT): (A) Sortable silt mass abundance from Sites U1406 and U1411. Bold lines represent moving averages superimposed on individual data points. Note site-specific scales to compare temporal trends. (B) Terrigenous (non-carbonate) mass accumulation rates for Sites U1406 and U1411. Note site-specific horizontal axes to compare temporal trends. (C) Lithogenic radiogenic isotopes from Site U1411. (D) Pb/Pb from detrital feldspar grains at Site U1411. Note separate scale $^{208}Pb/^{204}Pb$. (E) Benthic foraminifera $\delta^{18}O$ isotope compilation from the Atlantic Ocean (Site 1263; Langton et al., 2015), the Southern Ocean (Site 689; Diester-Haass & Zahn, 1996; and Site 744; Zachos et al., 1996), and the Pacific Ocean (Site 1218; Coxall and Wilson, 2011). (F) Sea surface temperature records from Site 647 (TEX_{86}); Śliwińska et al., 2023) and nearby Site U1404 (alkenones; Liu et al., 2018); open circles are data points with low alkenone concentration. Eocene-Oligocene Transition (EOT), earliest

Oligocene oxygen isotope step (EOIS), and Eocene-Oligocene boundary (EOB) as defined by Hutchinson et al. (2021) shown.

Fig. 7: (A) Sortable silt mass abundance (SS%) with 4-point moving average (bold lines) and (B) time-averaged SS% in 500-kyr age bins for Sites U1406 (red) and U1411 (black) compared to (C) global benthic $\delta^{18}O$ record (Westerhold et al., 2020), (D) sea surface temperature (SST) record from nearby Site U1404 (Liu et al., 2018); open circles are data points with low alkenone concentrations and points are connected/disconnected as originally displayed by Liu et al. (2018), and (E) pCO_2 proxy record (showing alkenone and boron; Foster et al., 2017) for 35-26 Ma time period. Eocene-Oligocene Transition (EOT) and earliest Oligocene oxygen isotope step (EOIS) as defined by Hutchinson et al. (2021) shown. Slump interval in Site U1406 as defined by van Peer et al. (2017) show in light red zone (A, B).

References Cited

Abelson, M., Agnon, A., Almogi-Labin, A. 2008. Indications for control of the Iceland plume on the Eocene-Oligocene "greenhouse-icehouse" climate transition. *Earth and Planetary Science Letters, 265,* 33048. doi:10.106/j.epsl.2007.09.021.

Abelson, M., Erez, J. 2017. The onset of modern-like Atlantic meridional overturning circulation at the Eocene-Oligocene transition: Evidence, causes, and possible implications for global cooling. *Geochemistry, Geophysics, Geosystems, 18,* 1-23. doi:10.002/2017GC006826.

Baker, J., Peate, D., Waight, T., Meyzen, C. 2004. Pb isotopic analysis of standards and samples using a $^{207}Pb/^{204}Pb$ double spike and thallium to correct for mass bias with a double-focuing MC- ICP-MS. *Chemical Geology, 3*(211), 275-303. doi:10.1016/j.chemgeo.2004.06.030.

Bianchi, G.G., Hall, I.R., McCave, I.N., Joseph, L. 1999. Measurement of the sortable silt current speed proxy using the SediGraph 5100 and Coulter Multisizer Iie: precision and accuracy. *Sedimentology*, 46, 1001-1014.

Böhm, E., Lippold, J., Gutjahr, M., Frank, M., Blaser, P., Antz, B., Fohlmeister, J., Frank, N., Andersen, M.B., Deininger, M. 2015. Strong and deep Atlantic meridional overturning circulation during the last glacial cycle. Nature, 517, 73-76. doi:10.1038/nature14059.

Borrelli, C., Cramer, B.S., Katz, M.E. 2014. Bipolar Atlantic deepwater circulation in the middle-late Eocene: Effects of Southern Ocean gateway openings. *Paleoceanography, 29*, 308-327. doi:10.1002/2012PA002444.

667 Boyle, P.R., Romans, B.W., Tucholke, B.E., Norris, R.D., Swift, S.A., Sexton, P.F. 2017.
668 Cenozoic North Atlantic deep circulation history recorded in contourite drifts, offshore
669 Newfoundland, Canada. *Marine Geology, 385,* 185-203. doi: 10.1016/j.margeo.2016.12.014.

670 Buckley, M.W., Marshall, J. 2016. Observations, inferences, and mechanisms of the Atlantic
671 Meridional Circulation: a review. *Reviews of Geophysics, 54,* 5-63. Doi:10.1002/2015RG00493.

672 Clark, P.U., Pisias, N.G., Stocker, T.F., Weaver, A.J. 2002. The role of thermohaline circulation
673 in abrupt climate change. *Nature, 415*(6874)*,* 863-869. Doi:10.1038/415863a.

674 Coakley, J.P., Syvitski, J.P.M. 1991. SediGraph technique. In J.P.M. Syvitski (Ed.), *Principles,*
675 *Methods and Application of Particle Size Analysis* (pp. 129-142). New York, Cambridge
676 University Press.

677 Coxall, H.K., Wilson, P.A. 2011. Early Oligocene glaciation and productivity in the eastern
678 equatorial Pacific: Insights into global carbon cycling. *Paleoceanography*, 26,
679 10.1029/2010PA002021

680 Coxall, H.K., Huck, C.E., Huber, M., Lear, C.H., Legarda-Lisarri, A., O'Regan, M., Śliwińska,
681 K.K., van de Flierdt, T., de Boer, A.M., Zachos, J.C., Backman, J. 2018. Export of nutrient rich
682 Northern Component Water preceded early Oligocene Antarctic glaciation. *Nature Geoscience,*
683 *11,* 190-196. https://doi.org/10/1038/s41561-018-0069-0.

684 Culp, J., Parent, A.M., Abolfazli, E., Strom, K., Romans, B.W. 2021. Advective sorting of silt by
685 currents: A laboratory study. *Sedimentology*. doi:10.1111/sed.12889.

686 Davies, R., Cartwright, J.A., Pike, J., Line, C. 2001. Early Oligocene initiation of North Atlantic
687 Deep Water Formation. *Nature, 410*(6831), 917-920*.* doi:10.1038/35073551.

688 Diester-Haass, L., Zahn, R. 1996. Eocene-Oligocene transition in the Southern Ocean: history of
689 water mass circulation and biological productivity. *Geology*, 24, 163-166.

690 Du, J., Haley, B.A., Mix, A.C. 2020. Evolution of the Global Overturning Circulation since the
691 Last Glacial Maximum based on marine authigenic neodymium isotopes. *Quaternary Science*
692 *Reviews, 241*, 106396. Doi:10.1016/j.quascirev.2020.106396.

693 Egger, L.M., Sliwinska, K.K., van Peer, T.E., Liebrand, D., Lippert, P.C., Friedrich, O., Wilson,
694 P.A., Norris, R.D., Pross, J. 2016. Magnetostratigraphically-calibrated dinoflagellate cyst
695 bioevents for the uppermost Eocene to lowermost Miocene of the western North Atlantic (IODP
696 Expedition 342, Paleogene Newfoundland sediment drifts). *Review of Palaeobotany and*
697 *Palynology*, doi: 10.1016/j.revpalbo.2016.08.002.

698 Elsworth, G., Galbraith, E., Halverson, G., Yang, S. 2017. Enhanced weathering and CO2
699 drawdown caused by latest Eocene strengthening of the Atlantic meridional overturning
700 circulation. *Nature Geoscience, 10,* 213-217. doi:10.1038/NGEO2888.

701 Faguéres, J.C., Stow, D.A.V., Imbert, P., Viana, A. 1999. Seismic features diagnostic of
702 contourite drifts. *Marine Geology, 162*(1), 1-38. https://doi.org/1016/S0025-3227(99)00068-7.

703 Fer, L., Voet, G., Seim, K.S., Rudels, B., Latarius, K. 2010. Intense mixing of the Faroe Bank
704 Channel overflow. *Geophysical Research Letters, 37*(02604), 1-5. doi:10.1029/2009GL041924.

705 Firth, J.V., Eldrett, J.S., Harding, I.C., Coxall, H.K., Wade, B.S. 2013. Integrated
706 biomagnetochronology for the Palaeogene of ODP Hole 647A: Implications for correlating
707 palaeoceanographic events from high to low latitudes. In *Magnetic Methods and the Timing of*
708 *Geologic Processes* (Jovane, L., Herrero-Bervera, E., Hinnov, L.A., and Housen, B.A., Eds.),
709 Geological Society, London, Special Publications, 373, 29-78.

710 Flood, R.D. 1988. A lee wave model for deep-sea mudwave activity. *Deep Sea Research Part A.*
711 *Oceanographic Research Papers, 35*(6), 973-983. doi: 10.1016/0198-0149(88)90071-4.

712 Foster, G.L., Royer, D., Lunt, D.J. 2017. Future climate forcing potentially without precedent in
713 the last 420 million years. *Nature Communications, 8*(14845), 1-8. doi:10.1038/ncomms14845.

714 Gradstein, F.M., Ogg, J.G. 2012. The Geologic Timescale 2012. Elsevier, Amsterdam.

715 Guitián, J., Phelps, S., Polissar, P.J., Ausin, B., Eglinton, T.I., Stoll, H.M. 2019. Midlatitude
716 temperature variations in the Oligocene to Early Miocene. *Paleoceanography and*
717 *Paleoclimatology*, 34, 1328-1343, doi: 10.1029/2019PA003638.

718 Haine, T., Böning, C., Brandt, P., Fischer, J., Funk, A., Kieke, D., Kvaleberg, E., Rhein, M.,
719 Visbeck, M. 2008. North Atlantic Deep Water formation in the Labrador Sea, recirculation
720 through the subpolar gyre, and discharge to the subtropics. In R.R. Dicskon, J. Meincke, P.
721 Rhines, (Eds.), *Arctic-Subarctic Ocean Fluxes* (pp. 653-701). Dordrecht, Netherlands, Springer.

722 Hohbein, M.W., Sexton, P.F., Cartwright, J.A. 2012. Onset of North Atlantic Deep Water
723 production coincident with inception of the Cenozoic global cooling trend. *Geology, 40*(3), 255-
724 258. doi:10.1130/G32461.1.

725 Hutchinson, D.K., Coxall, H.K., O'Regan, M., Nilsson, J., Caballero, R., de Boer, A.M. 2019.
726 Arctic closure as a trigger for Atlantic overturning at the Eocene-Oligocene Transition. *Nature*
727 *Communications, 10*(3797), 1-9. doi:10.1038/s41467-019-11828-z.

728 Hutchinson, D.K., Coxall, H.K., Lunt, D.J., Steinthorsdottir, M., De Boer, A.M., Baatsen, M.,
729 von der Heydt, A., Huber, M., Kennedy-Asser, A.T., Kunzmann, L., Ladant, J-B, Lear, C.H.,
730 Moraweck, K., Pearson, P.N., Piga, E., Pound, M.J., Salzmann, U., Scher, H.D., Sijp, W.P.,
731 Śliwińska, K.K., Wilson, P.A., Zhang, Z. 2021. The Eocene-Oligocene transition: a review of
732 marine and terrestrial proxy data, models and model-data comparisons. *Climate of the Past, 17*,
733 269-315. doi:10.5194/cp-17-269-2021.

734 Kaminski, M., Ortiz, S. 2014. The Eocene-Oligocene turnover of Deep-Water Agglutinated
735 Foraminifera at ODP Site 647, Southern Labrador Sea (North Atlantic). *Micropaleontology*, 60,
736 53-66.

737 Kostov, Y., Armour, K.C., Marshall, J. 2014. Impact of the Atlantic meridional overturning
738 circulation and tranisent climate change. *Geophysical Research Letters, 41*, 2108-2116.
739 doi:10.1002/2013GL058998.

740 Langton, S.J., Rabideaux, N.M., Borelli, C., Katz, M.E. 2016. Southeastern Atlantic deep-water
741 evolution during the late-middle Eocene to earliest Oligocene (Ocean Drilling Program Site 1263
742 and Deep Sea Drilling Project Site 366). *Geosphere, 12*(3), 1032-1047. doi:
743 10.1130/GES01268.1.

744 Ledbetter, M.T.. 1986. A Late Pleistocene time-series of bottom-current speed in the Vema
745 Channel. *Palaeogeography, Palaeoclimatology, Palaeoecology, 53*, 97–105. doi:10.1016/0031-
746 0182(86)90040-4.

747 Liu, Z., He, Y., Jiang, Y., Wang, H., Liu, W., Bohaty, S.M., Wilson, P.A. 2018. Transient
748 temperature asymmetry between hemispheres in the Palaeogene Atlantic Ocean. *Nature*
749 *Geoscience, 11*, 656-660. doi: 10.1038/s41561-018-012-9.

750 Lynch-Stieglitz, J., Curry, W.B., Slowey, N. 1999. A geostrophic transport estimate for the
751 Florida Current from the oxygen isotope composition of benthic foraminifera.
752 *Paleoceanogarphy*, 14, 360-373.

753 McCave, I.N., Tucholke, B.E. 1986. Deep current-controlled sedimentation in the western North
754 Atlantic. In P.R. Vogt, B.E. Tucholke (Eds.), *The Geology of North America, The Western North*
755 *Atlantic Region* (Vol. M, pp. 451-468). Boulder, CO, The Geological Society of America.

756 McCave, I.N., Manighetti, B., Robinson, S.G. 1995. Sortable silt and fine sediment
757 size/composition slicing: Parameters for paleocurrent speed and paleoceanography.
758 *Paleoceanography, 10*(3), 593-610. doi: 10.1029/94PA03039.

McCave, I.N., Hall, I.R. 2006. Size sorting in marine muds: Processes, pitfalls, and prospects for paleoflow-speed proxies. *Geochemistry, Geophysics, Geosystems, 7*(10), 1-37, doi:10.1029/2006GC001284.

McCave, I.N., Thornalley, D.J.R., Hall, I.R. 2017. Relation of sortable silt grain-size to deep-sea current speeds: Calibration of the 'Mud Current Meter.' *Deep-Sea Research Part I, 127,* 1-12. doi: 10.1016/j.dsr.2017.07.003.

McCave, I.N., Andrews, J.T. 2019. Distinguishing current effects in sediments delivered to the ocean by ice. I. Principles, methods and examples. *Quaternary Science Reviews*, 212, 92-107, doi: 10.106/j.quascirev.2019.03.031.

Miller, K.G., Gradstein, F.M., Berggren, W.A. 1982. Late Cretaceous to Early Tertiary Agglutinated Benthic Foraminifera in the Labrador Sea. *Micropaleontology*, 28, 1-30.

Miller, K.G., Browning, J.V., Schmelz, W.J., Kopp, R.E., Mountain, G.S., Wright, J.D. 2020. Cenozoic sea-level and cryospheric evolution from deep-sea geochemical and continental margin records. *Science Advances,* 6. doi:10.1126/sciadv.aaz1346.

Mountain, G.S., Miller, K.G. 1992. Seismic and geologic evidence for Early Paleogene deepwater circulation in the western North Atlantic. *Paleoceanography, 7*(4), 423-429. doi:10.1029/92PA01268.

Mountain, G.S., Tucholke, B.E. 1985. Mesozoic and Cenozoic Geology of the U.S. Atlantic Continental Slope and Rise. In C.W. Poag (Ed.), *Geologic Evolution of the U.S. Atlantic Margin* (pp. 293-341). Stroudsburg, PA, Van Nostrand Reinhold.

Nicolo, M.J., Dickens, G.R. 2006. Data report: terrigenous grain-size distributions at Sites 1263 and 1267: testing the applicability of Leg 208 sediments for eolian analysis. *Proc. Ocean Drilling Program, 208 Scientific Results*, 208. doi: 10.2973/odp.proc.sr.208.205.2006.

Norris, R.D., Wilson, P.A., Blum, P., Fehr, A., Agini, C., Bornemann, A., Boulila, S., Bown, P.R., Cournede, C., Friedrich, O., Ghosh, A.K., Hollis, C.J., Hull, P.M., Jo, K., Junium, C.K., Kaneko, M., Liebrand, D., Lippert, P.C., Liu, Z., Matsui, H., Moriya, K., Nishi, H., Opdyke, B.N., Penman, D., Romans, B., Scher, H.D., Sexton, P., Takagi, H., Turner, S.K., Whiteside, J.H., Yamaguchi, T., Yamamoto, Y. 2014a. Expedition 342 summary. In Norris, R.D., Wilson, P.A., Blum, P. (Eds.), *Proc. IODP* (Vol. 342). College Station, TX, Integrated Ocean Drilling Program. doi:10.2204/iodp.proc.342.101.2014.

Norris, R.D., Wilson, P.A., Blum, P., Fehr, A., Agini, C., Bornemann, A., Boulila, S., Bown, P.R., Cournede, C., Friedrich, O., Ghosh, A.K., Hollis, C.J., Hull, P.M., Jo, K., Junium, C.K., Kaneko, M., Liebrand, D., Lippert, P.C., Liu, Z., Matsui, H., Moriya, K., Nishi, H., Opdyke,

792 B.N., Penman, D., Romans, B., Scher, H.D., Sexton, P., Takagi, H., Turner, S.K., Whiteside,
793 J.H., Yamaguchi, T., Yamamoto, Y. 2014b. Site 1406. In Norris, R.D., Wilson, P.A., Blum, P.
794 (Eds.), *Proc. IODP* (Vol. 342). College Station, TX, Integrated Ocean Drilling Program.
795 doi:10.2204/iodp.proc.342.107.2014.

796 Norris, R.D., Wilson, P.A., Blum, P., Fehr, A., Agini, C., Bornemann, A., Boulila, S., Bown,
797 P.R., Cournede, C., Friedrich, O., Ghosh, A.K., Hollis, C.J., Hull, P.M., Jo, K., Junium, C.K.,
798 Kaneko, M., Liebrand, D., Lippert, P.C., Liu, Z., Matsui, H., Moriya, K., Nishi, H., Opdyke,
799 B.N., Penman, D., Romans, B., Scher, H.D., Sexton, P., Takagi, H., Turner, S.K., Whiteside,
800 J.H., Yamaguchi, T., Yamamoto, Y. 2014c. Site 1411. In Norris, R.D., Wilson, P.A., Blum, P.
801 (Eds.), *Proc. IODP* (Vol. 342). College Station, TX, Integrated Ocean Drilling Program.
802 doi:10.2204/iodp.proc.342.112.2014.

803 Parnell-Turner, R., White, N.J., McCave, I.N., Henstock, T.J., Murton, B., Jones, S.M. 2015.
804 Architecture of North Atlantic contourite drifts modified by transient circulation of the Icelandic
805 mantle plume. *Geochemistry, Geophysics, Geosystems,* 16, 3414-3435, doi:
806 10.1002/2015GC005947.

807 Pe-Piper, G., Piper, D.J.W., Jansa, L.F., de Jonge, A., 2007, Early Cretaceous opening of the
808 North Atlantic Ocean: Implications of the petrology and tectonic setting of the Fogo Seamounts
809 off the SW Grand Banks, Newfoundland. *GSA Bulletin, 119*(5-6), 712-724. doi:10.1130/B26008.

810 Poore, H.R., Samworth, R., White, N.J., Jones, S.M., McCave, I.N. 2006. Neogene overflow of
811 Northern Component Water at the Greenland-Scotland Ridge. *Geochemistry, Geophysics,*
812 *Geosystems*, 7, doi: 10.1029/2005GC001085.

813 Posamentier, H.W., Erskine, R.D., and Mitchum, R.M., Jr., 1991, Submarine fan depositions
814 within a sequence stratigraphic framework, in Welmer, B. and Link, M.H., eds., *Seismic facies*
815 *and sedimentary processes of submarine fans and turbidite systems*: New York, Springer-Verlag,
816 127-136

817 Rebesco, M., Hernández-Molina, F.J., Van Rooji, D., Wåhlin, A. 2014. Contourites and
818 associated sediments controlled by deep-water circulation processes: State-of-the-art and future
819 considerations. *Marine Geology, 352,* 111-154. doi: 10.1016/j.margeo.2014.03.011.

820 Scher, H.D., Martin, E.E. 2006. Timing and climatic consequences of the opening of Drake
821 Passage. *Science, 312*(5772), 428-430. doi:10.1126/science.1120044.

822 Scher, H.D., Bohaty, S.M., Zachos, J.C., Delaney, M.L. 2011. Two-stepping into the icehouse:
823 East Antarctic weathering during progressive ice-sheet expansion at the Eocene-Oligocene
824 transition. *Geology, 39*, 4, 383-386. Doi:10.1130/G31726.

825 Scher, H.D., Whittaker, J.M., Williams, S.E., Latimer, J.C., Kordesch, W.E.C., Delaney, M.L.
826 2015. Onset of Antarctic Circumpolar Current 30 million years ago as Tasmanian Gateway
827 aligned with westerlies. *Nature, 523*, 580-583. doi:10.1038/nature14598.

828 Scher, H. 2017. Carbon-ocean gateway links. *Nature Geoscience, 10*, 164-165. 802

829 Sijp, W.P., England, M.H. 2004. Effect of Drake Passage throughflow on global climate. *Journal*
830 *of Physical Oceanography, 34,* 1254-1256.

831 Sijp, W.P., England, M.H., Huber, M. 2011. Effect of the deepening of the Tasman Gateway on
832 the global ocean. *Paleoceanography, 26*(4207), 1-18. doi:10.1029/2011PA002143.

833 Śliwińska, K.K., Coxall, H.K., Hutchinson, D.K., Liebrand, D., Schouten S., de Boer, A.M.
834 2023. Sea surface temperature evolution of the North Atlantic Ocean across the Eocene-
835 Oligocene transition. *Climate of the Past*, 19, 123-140. doi: 10.5194/cp-19-123-2023

836 Spray, J.F., Bohaty, S.M., Davies, A., Bailey, I., Romans, B.W., Cooper, M.J., Milton, J.A.,
837 Wilson, P.A. 2019. North Atlantic evidence for a unipolar icehouse climate state at the Eocene-
838 Oligocene Transition. *Paleoceanography and Paleoclimatology, 34*, 1-15.
839 doi:10.1029/2019PA003563

840 Stow, D.A.V., Hunter, S., Wilkinson, D., Hernández-Molina, F.J. 2008. The nature of contourite
841 deposition. In *Contourites* (Rebesco, M. & Camerlenghi, A., Eds.), *Developments in*
842 *Sedimentology, 60*, 143-156, Elsevier, Amsterdam. doi:10.1016/S0070-4571(08)10009-7.

843 Straume, E.O., Gaina, C., Medvedev, Nisancioglu, K.H. 2020. Global Cenozoic paleobathymetry
844 with a focus on the Northern Hemisphere oceanic gateways. *Gondwana Research, 86,* 126-143.
845 doi:10.1016/j.gr.2020.05.011.

846 Straume, E.O., Nummelin, A., Gaina, C., Niscancioglu, K.H. 2022. Climate transition at the
847 Eocene-Oligocene influenced by bathymetric changes to the Atlantic-Arctic oceanic gateways.
848 *Proceedings of the National Academy of Sciences*, 119, doi: 10.1073/pnas.2115346119.

849 Taylor, R.N., Ishizuka, O., Michalik, A., Milton, J.A., Croudace, I.W. 2015. Evaluating the
850 precision of Pb isotope measurement by mass spectrometry. *Journal of Analytical Atomic*
851 *Spectrometry, 30*(1), 198-213. doi:10.1039/C4JA00279B.

852 Thornalley, D.J.R., Oppo, D.W., Ortega, P., Robson, J.I., Brierley, C.M., Davis, R., Hall, I.R.,
853 Moffa-Sanchez, P., Rose, N.L., Spooner, P.T., Yashayaev, I., Keigwin, L.D. 2018. Anomalously
854 weak Labrador Sea convection and Atlantic overturning during the past 150 years. *Nature, 556*,
855 doi:10.1038/s41586-018-0007-4.

Trenberth, K.E., Caron, J.M. 2001. Estimates of meridional atmosphere and ocean heat transports. *Journal of Climate*, 14, 3433-3443. doi: 10.1175/1520-0442(2001)014.

Uenzelmann-Neben, G., Gruetzner, J. 2018. Chronology of Greenland Scotland Ridge overflow: What do we really know? *Marine Geology*, 406, 109-118.

Vahlenkamp, M., Niezgodzki, I., De Vleeschouwer, D., Lohmann, G., Bickert, T., Pälike, H. 2018. Ocean and climate response to North Atlantic seaway changes at the onset of long-term Eocene cooling. *Earth and Planetary Science Letters, 498,* 185-195. doi: 10.1016/j.epsl.2018.06.031.

van Peer, T.E., Xuan, C., Lippert, P.C., Liebrand, D., Agnini, C., Wilson, P.A. 2017. Extracting a detailed magnetostratigraphy from weakly magnetized, Oligocene to Early Miocene sediment drifts recovered at IODP Site U1406 (Newfoundland margin, northwest Atlantic Ocean). *Geochemistry, Geophysics, Geosystems*, 18, 3910-3928

Via, R.K., Thomas, D.J. 2006. Evolution of Atlantic thermohaline circulation: Early Oligocene onset of deep-water production in the North Atlantic. *Geology, 34*(6), 441-444. doi:10.1130/G22545.1. doi: 10.1002/2017GC007185.

Vogt, P.R., 1972. The Faeroe-Iceland-Greenland aseismic ridge and the western boundary undercurrent. *Nature*, 239, 79-81.

Wold, C.N. 1994. Cenozoic sediment accumulation on drifts in the northern North Atlantic. *Paleoceanography, 9*(6), 917-941.

Wright, J.D., Miller, K.G. 1993. Southern Ocean influences on late Eocene to Miocene deepwater circulation. *Antarctic Research Series, 60,* 1-25.

Wright, J.D., Miller, K.G. 1996. Control of North Atlantic Deep Water circulation by the Greenland-Scotland Ridge. *Paleoceanography, 11,* 157-170.

Zachos, J.C., Breza, J., Wise, S.W. 1992, Early Oligocene ice-sheet expansion on Antarctica: Stable isotope and sedimentological evidence from Kerguelen Plateau, southern Indian Ocean: *Geology, 20,* 569–573, doi: 10.1130/0091-7613(1992)020<0569:EOISEO >2.3.CO;2.

Zachos, J.C., Quinn, T.M., Salamy, K.A. 1996. High-resolution (10^4 years) deep-sea foraminiferal stable isotope records of the Eocene-Oligocene climate transition. *Paleoceanography*, 11, 251-266.

885 Zickfield, K., Levermann, A., Morgan, M.G., Kuhlbrodt, T., Rahmstorf, S., Keith, D.W. 2007.
886 Expert judgements on the response of the Atlantic meridional overturning circulation to climate
887 change. *Climatic Change, 82*(3-4), 235-265. doi:10.1007/s10584-007-9246-3.

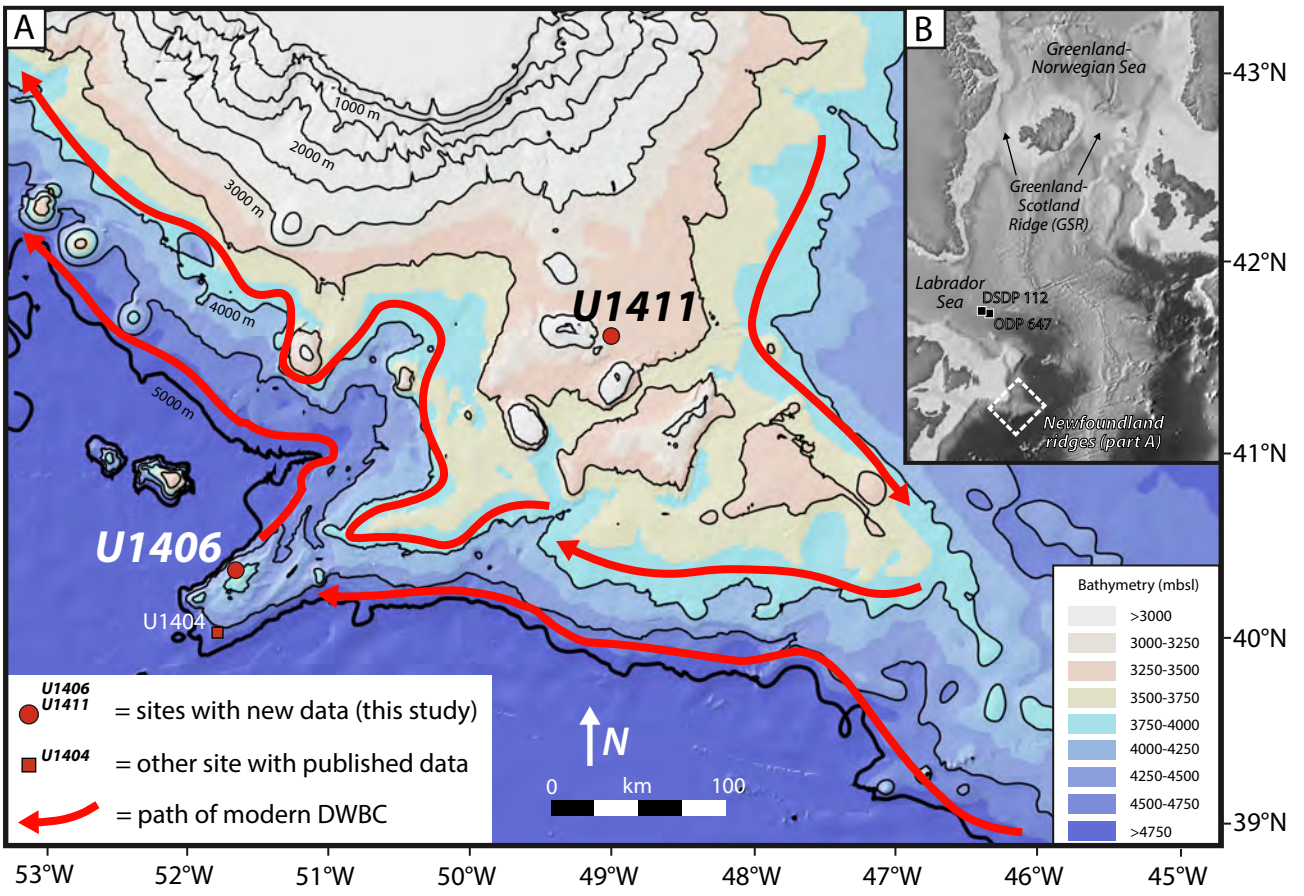

Fig. 1: (A) Bathymetric map of Newfoundland Ridges drift complex, offshore Canada, showing location of new terrigenous grain-size data reported in this study from Sites U1411 and U1406 (from IODP Exp 342). Approximate path and depth range of modern Deep Western Boundary Current (DWBC) annotated by red arrows. (B) Inset showing expanded view of the northern North Atlantic Ocean, southern Labrador Sea, the Greenland-Scotland Ridge (GSR), and Greenland-Norwegian Sea. Part A designated by dashed white box. Note location of other sites with published data referenced in the text. Maps generated using http://www.geomapapp.org/

Figure 1 – Parent et al.

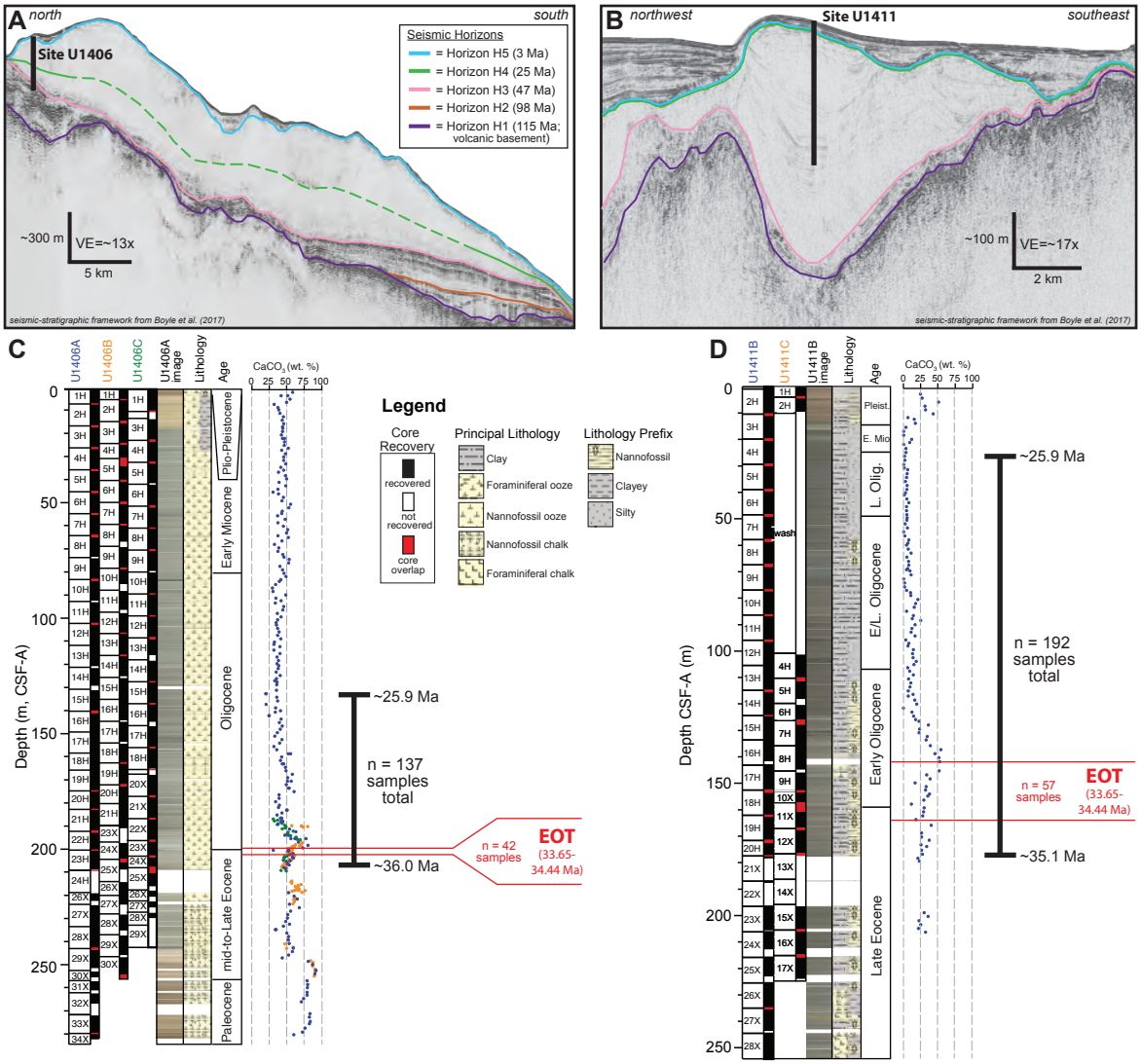

Figure 2: Seismic-stratigraphic and lithologic context for IODP Sites U1406 and U1411 and associated analyzed samples. (A) Seismic-reflection profile (Line 5), including horizon interpretation from Boyle et al. (2017), showing Site U1406 location. (B) Seismic-reflection profile (Line 25), including horizon interpretation from Boyle et al. (2017), showing Site U1411. Key to seismic-stratigraphic horizon colors for both profiles. (C) Summary of Site U1406 and (D) of Site U1411, both showing core recovery, lithology, general age, and shipboard $CaCO_3$% information (from Norris et al., 2014b; Norris et al., 2014c). Stratigraphic distribution of samples with the EOT (Eocene-Oligocene Transition) interval, per Hutchinson et al. (2021), shown in red.

Figure 2 – Parent et al.

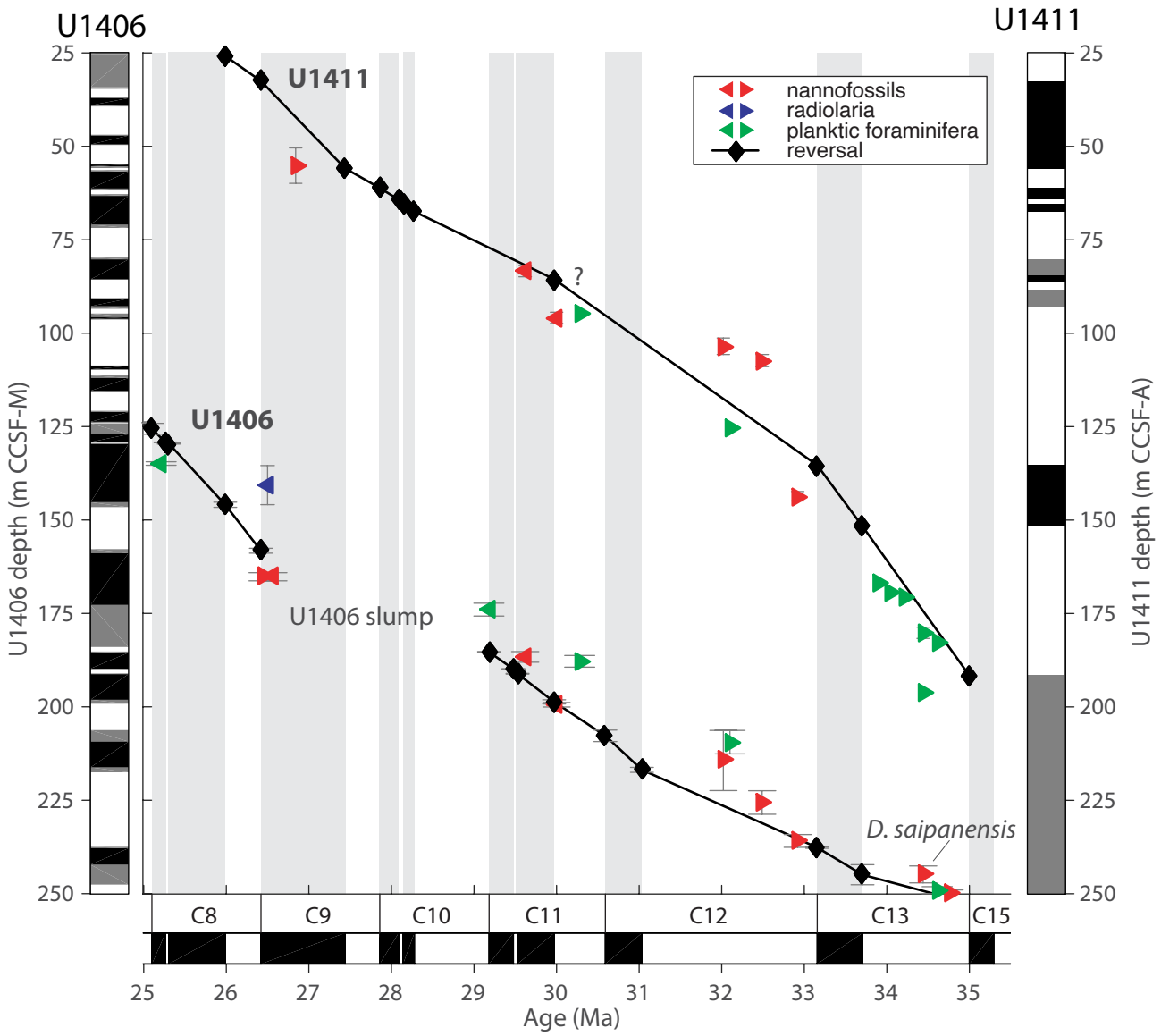

Fig. 3: Age models for IODP Sites U1406 and U1411 constructed using biostratigraphic and magneto-stratigraphic tie points (Norris et al., 2014b, 2014c; van Peer et al., 2017). From left to right: magneto-stratigraphy of Site U1406, depth-age tie points used in this study, and magnetostratigraphy of Site U1411. Question mark (?) denotes interval where paleomagentic age constraint is less clear. Magneto-stratigraphies are correlated to the Geomagnetic Polarity Time Scale (Gradstein and Ogg, 2012) across the bottom of the plot.

Figure 3 – Parent et al.

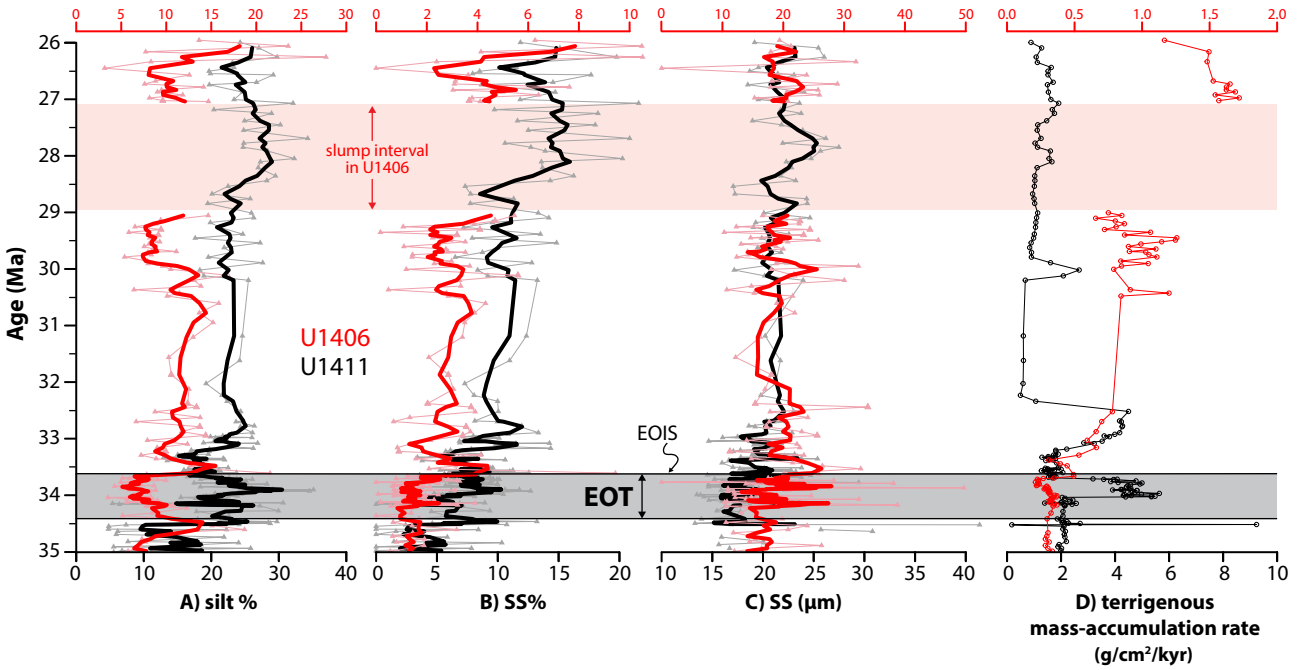

Fig. 4: Terrigenous grain-size data. (A) Mass abundance of silt (4-63 µm fraction). (B) mass abundance of sortable silt (10-63 µm). (C) Mean sortable silt (mean diameter of 10-63 µm fraction). Parts A-C have a 4-point moving average superimposed on data. D) Terrigenous (non-carbonate) mass accumulation rates. U1406 (red) and U1411 (black) for all panels. Eocene-Oligocene Transition (EOT) and earliest Oligocene oxygen isotope step (EOIS) as defined by Hutchinson et al. (2021) shown.

Figure 4 – Parent et al.

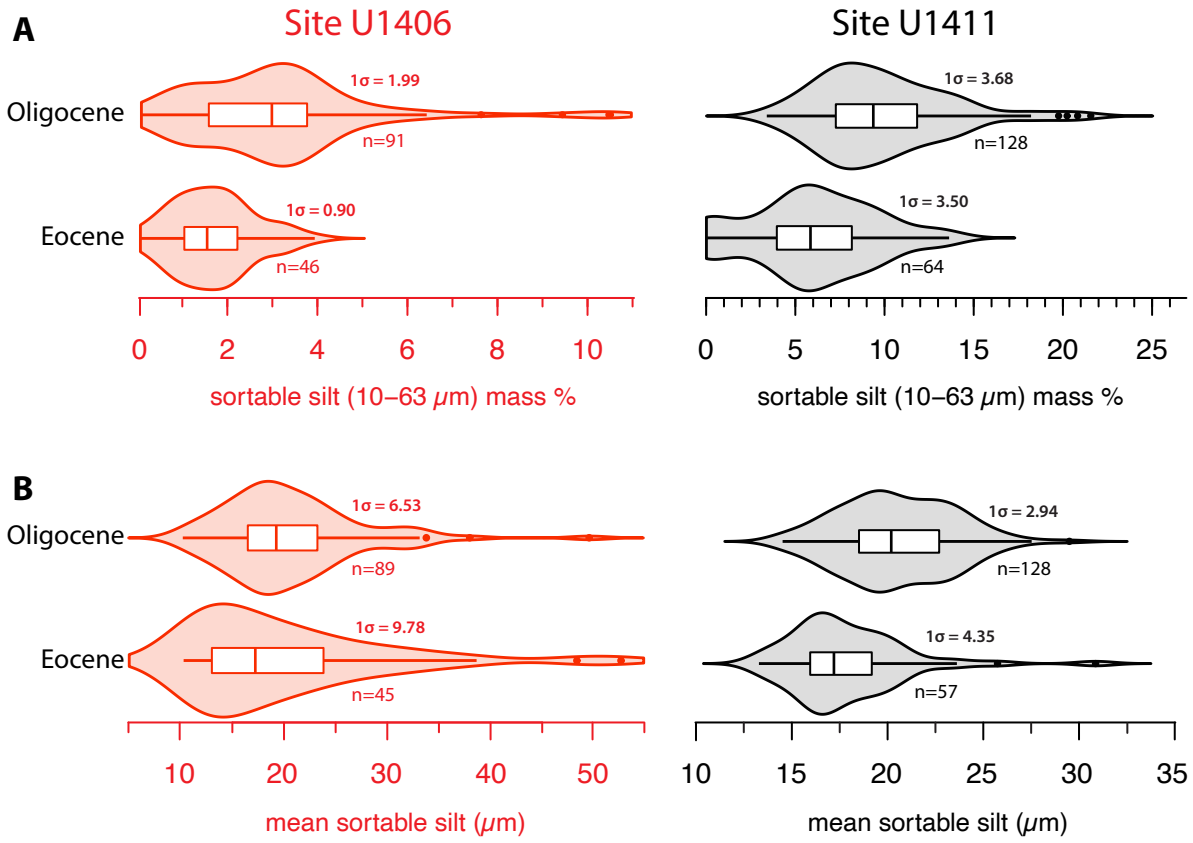

Figure 5: Violin plots (mirror-image density curves) with boxplot overlay of terrigenous (A) sortable silt (10-63 μm) mass %, and (B) mean sortable silt for Sites U1406 and U1411 subdivided into Eocene versus Oligocene (using Eocene-Oligocene boundary of 33.9 Ma). Boxplots show interquartile range (white fill) and median (vertical line). Annotation denotes standard deviation and number of data points.

Figure 5 – Parent et al.

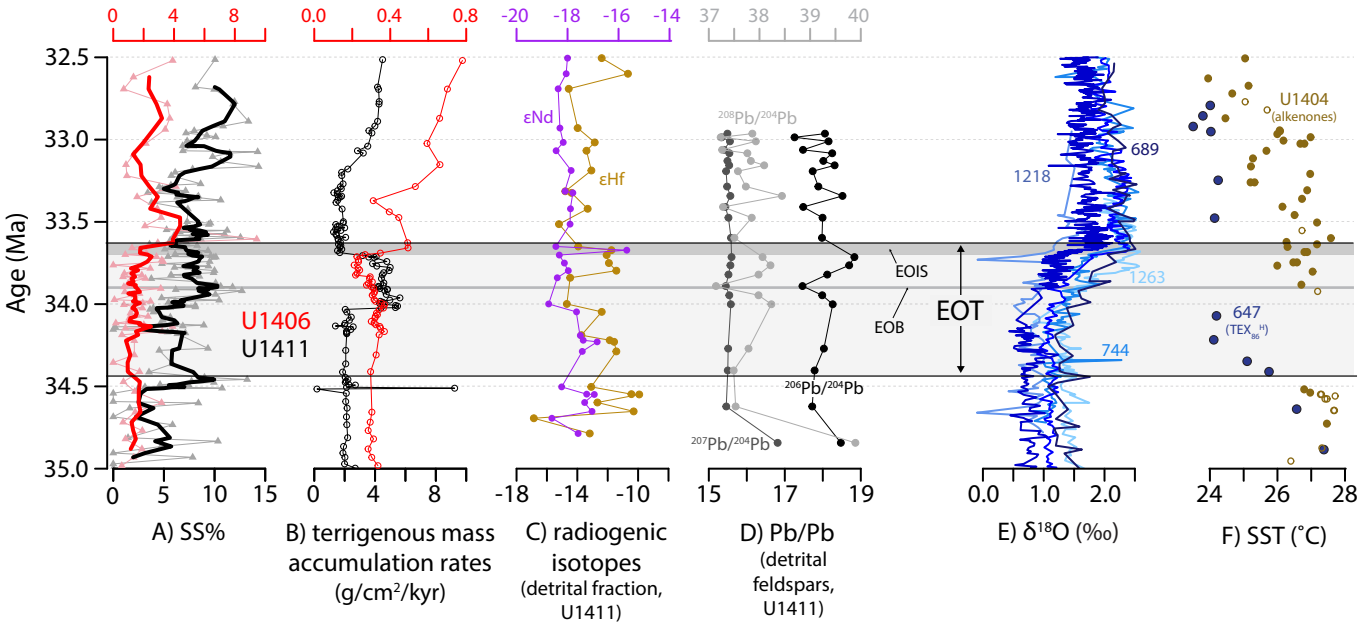

Fig. 6: Multi-proxy record across the Eocene-Oligocene Transition (EOT). (A) Sortable silt mass abundance from Sites U1411 and U1406. Bold lines represent moving averages superimposed on individual data points. Note site-specific scales to compare temporal trends. (B) Terrigenous (non-carbonate) mass accumulation rates for Sites U1411 and U1406. Note site-specific horizontal axes to compare temporal trends. (C) Lithogenic radiogenic isotopes from Site U1411. (D) Pb/Pb from detrital feldspar grains at Site U1411. Note separate scale for $^{208}Pb/^{204}Pb$. (E) Benthic foraminifera $\delta^{18}O$ isotope compilation from the Atlantic Ocean (Site 1263; Langton et al., 2015), Southern Ocean (Site 689; Diester-Haass and Zhan, 1996; and Site 744; Zachos et al., 1996), and the Pacific Ocean (Site 1218; Coxall and Wilson, 2011). (F) Sea surface temperatures records from Site 647 (TEX_{86}; Sliwinska et al. 2023) and nearby Site U1404 (alkenones; Liu et al., 2018); open circles are data points with low alkenone concentration. Eocene-Oligocene Transition (EOT), earliest Oligocene oxygen isotope step (EOIS), and Eocene-Oligocene boundary (EOB) as defined by Hutchinson et al. (2021) shown.

Figure 6 – Parent et al.

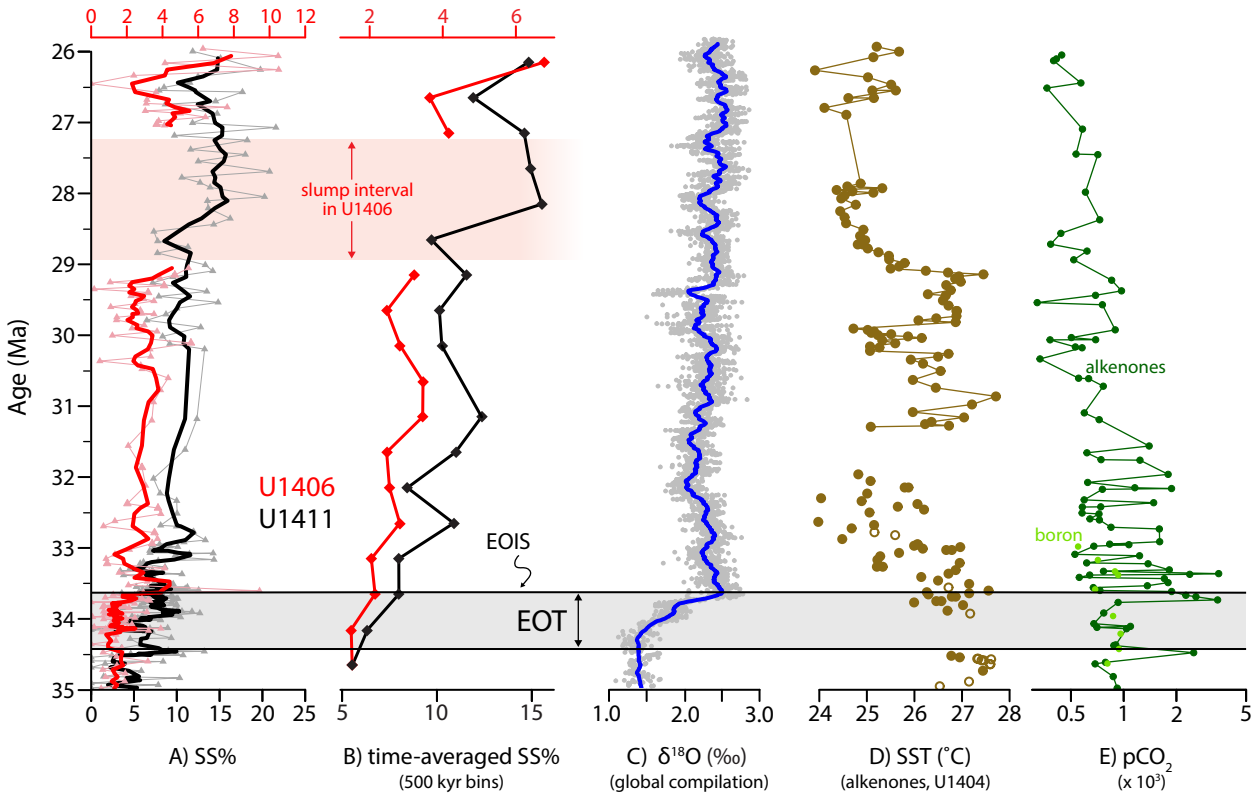

Figure 7: (A) Sortable silt mass abundance (SS%) with 4-point moving average (bold lines) and (B) time-averaged SS% in 500-kyr age bins for Sites U1406 (red) and U1411 (black) compared to (C) global benthic $\delta^{18}O$ compilation (Westerhold et al., 2020), (D) sea surface temperature (SST) record from nearby Site U1404 (Liu et al., 2018); open circles are data points with low alkenone concentrations and points are connected/disconnected as originally displayed by Liu et al. (2018), and (E) pCO_2 proxy record (showing alkenone and boron; Foster et al., 2017) for 35-26 Ma time period. Eocene-Oligocene Transition (EOT) and earliest Oligocene oxygen isotope step (EOIS) as defined by Hutchinson et al. (2021) shown. Slump interval in Site U1406 as defined by van Peer et al. (2018) shown in light red zone (A, B).

Figure 7 – Parent et al.